



# Contribution of buoyancy fluxes to tropical Pacific sea level variability

Patrick Wagner<sup>1</sup>, Markus Scheinert<sup>1</sup>, and Claus W. Böning<sup>1</sup>

<sup>1</sup>GEOMAR Helmholtz Centre for Ocean Research Kiel, Kiel Germany

**Correspondence:** Patrick Wagner (pwagner@geomar.de)

**Abstract.** Regional anomalies of steric sea level are either due to redistribution of heat and freshwater anomalies or due to ocean–atmosphere buoyancy fluxes. Interannual to decadal variability in sea level across the tropical Pacific is mainly due to steric variations driven by wind stress anomalies. The importance of air–sea buoyancy fluxes is less clear. We use a global, eddy permitting ocean model and a series of sensitivity experiments with quasi–climatological momentum and buoyancy fluxes to identify the contribution of buoyancy fluxes for interannual to decadal sea level variability in the tropical Pacific. We find their contribution on interannual timescales to be strongest in the central tropical Pacific at around 10° latitude in both hemispheres and also relevant in the very east of the tropical domain. Buoyancy flux forced anomalies are in phase with variations driven by wind stress changes but their effect on the prevailing anomalies and the importance of heat and fresh water fluxes vary locally. In the eastern tropical basin interannual sea level variability is amplified by anomalous heat fluxes, while the importance of fresh water fluxes is small and neither has any impact on decadal timescales. In the western tropical Pacific the variability on interannual and decadal timescales is dampened by both, heat and freshwater fluxes. The mechanism involves westward propagating Rossby waves that are triggered during ENSO events by anomalous buoyancy fluxes in the central tropical Pacific and counteract the prevailing sea level anomalies once they reach the western part of the basin.

## 1 Introduction

Sea level is an integrated measure that contains information about the water column as well as about ocean–atmosphere interaction. Global mean sea level variability (GMSL) is usually separated into two processes. Changes in the ocean’s total mass due to melting of land ice and changes of the density of the water column which are associated with changes of subsurface temperature and salinity distributions. Sea level variability is not spatially uniform (e.g. Stammer et al. 2013). Instead, it is influenced by ocean dynamics that act to redistribute ocean mass, heat and freshwater (e.g. Zanna et al. 2019). These redistributions leave the GMSL unaffected but can have strong impacts on regional scales rendering the spatial patterns of sea level variability highly non–uniform (e.g. Merrifield and Maltrud 2011). Ocean–atmosphere buoyancy fluxes can additionally modulate spatial patterns of sea level variability (e.g. Piecuch and Ponte 2012; Forget and Ponte 2015).

The tropical Pacific is a prominent example for an area where regional SLC substantially deviates from the GMSL. Between 1993 and roughly 2012 sea level rise in the western part of the basin was three times as strong as the global mean rate, while



the eastern basin saw no or even negative trends. These anomalies have been attributed to gradually increasing trade winds since the early 1990s (Merrifield and Maltrud, 2011). As such they are part of a multidecadal pattern of variability, that can be related to climate modes such as PDO, ENSO and SOI (Merrifield et al., 2012).

30 While it seems clear that the better part of sea level variability in the tropical Pacific is due to adiabatic processes and can be understood in terms of redistribution of heat driven by wind stress changes (Timmermann et al., 2010; Piecuch and Ponte, 2011; Merrifield, 2011; Merrifield and Maltrud, 2011; McGregor et al., 2012; Merrifield et al., 2012; Moon and Tony Song, 2013; Moon et al., 2013; Qiu and Chen, 2012), the importance of buoyancy fluxes is still under debate. Only a few studies have addressed the importance of diabatic processes for SLC in the region. Piecuch and Ponte (2011) assessed the contribution of  
35 surface buoyancy fluxes to steric SLC and identified a few regions where the contribution of local buoyancy fluxes is not negligible. One of them is the warm pool region in the western tropical Pacific. Other studies identified the central tropical Pacific as another region where local buoyancy fluxes contribute to interannual sea level variability (Piecuch and Ponte, 2012; Forget and Ponte, 2015; Meyssignac et al., 2017). Piecuch et al. (2019) argue that local, latent heatfluxes are in particular relevant on decadal timescales and contributed to the recent reversal of sea level trends in the tropical Pacific since 2012. All these studies  
40 used either local budget calculations or ocean model sensitivity simulations to estimate the contribution of buoyancy fluxes. Fukumori and Wang (2013) chose a different approach in a semi-Lagrangian model study and found buoyancy fluxes to be the dominant driver of sea level trends between 1993 and 2004 in the western Pacific warm pool.

A detailed assessment of the relative contribution of buoyancy flux anomalies to sea level variability in the region is impor-  
45 tant for projecting future sea level trends in this region, since adiabatic and diabatic forcing mechanism might evolve rather differently. However, in particular for the pre-altimetry era and on decadal timescales, we currently lack a detailed picture on how buoyancy fluxes affect sea level in the tropical Pacific and which mechanisms are involved. By means of eddy-permitting ocean model experiments that allows us to individually apply buoyancy and momentum flux forcing to the underlying ocean and by decomposing the steric sea level component into thermosteric and halosteric contributions, we assess the importance  
50 of buoyancy fluxes on interannual to decadal SLC over the last 6 decades, analyze their interplay with the wind stress driven variability and determine the importance of heat vs. fresh water fluxes.

## 2 Model experiments

We use a global ocean circulation model (OGCM) configuration of the "Nucleus for European Modelling of the Ocean" (NEMO) code version 3.6 (Madec and NEMO-team, 2016). The model uses a global tri-polar ORCA grid at 1/4° horizontal  
55 resolution. The vertical grid consists of 46 z-levels with varying layer thickness from 6 m at the surface to 250 m in the deepest levels. Bottom topography is interpolated from 2-Minute Gridded Global Relief Data ETOPO2v2<sup>1</sup> and represented by partial steps (Barnier et al., 2006). The model is forced with the JRA55-do forcing (Tsujino et al., 2018) which builds on the JRA55

<sup>1</sup><http://www.ngdc.noaa.gov/mgg/global/relief/ETOPO2/ETOPO2v2-2006/ETOPO2v2g/>



reanalysis product but is adjusted relative to observational datasets.

Laplacian and bilaplacian operators are used to parameterize horizontal diffusion of tracer and momentum respectively. The  
60 ocean model is coupled to the Louvain–La-Neuve sea–ice Model version 2 (LIM2–VP, (Fichefet and Maqueda, 1997).

To avoid spurious drifts of global freshwater content, all models use a sea surface salinity restoring with Piston velocities of 137  
mm per day, which corresponds to a relaxation timescales of one year for the upper 50 m, and a freshwater budget correction,  
that sets changes in the global budget to zero at each model timestep.

65 In addition to a hindcast simulation (O025-HC) that uses realistic, interannual forcing and is integrated from 1958 to 2016,  
two sensitivity experiments with interannual variability only in the momentum (O025-W90) or buoyancy fluxes (O025-B90)  
were conducted. As a means to construct a "quasi-climatological" forcing, we followed the approach of a "Repeated Year Forc-  
ing" (Stewart et al., 2020) to construct quasi-climatological atmospheric fields in order to compute buoyancy and momentum  
fluxes for the two sensitivity experiments. Following the recommendation of Stewart et al. (2020), we used the period from  
70 Mai 1990 to April 1991 repeatedly for 59 cycles to match the length of the hindcast. The three experiments have been used  
previously for studies of Indian Ocean heat content (Ummenhofer et al., 2020) and marine heatwaves (Ryan et al., 2021).

Interannual sea surface height<sup>2</sup> (SSH) variability from the model hindcast compares well with observations. Figure 1 shows  
interannual SSH variability as observed by satellite altimetry<sup>3</sup> and simulated by the OGCM. Because the boussinesq model  
75 used here does not capture the GMSL signal and the freshwater budget correction forces the GMSL anomaly to zero, the global  
mean signal has been removed from the altimetry data. The domain is characterized by the well-known meridional dipole with  
its eastern pole centered on the equator in the central to eastern Pacific. The western pole shows two maxima located around  
10° S and 10° N in the western part of the basin. Observations show amplitudes of up to 10 cm in the west and around 6 cm in  
the east (Fig. 1a). Overall, this structure is well captured by the model experiment, although the overall strength of the dipole is  
80 slightly underestimated with amplitudes of 8 cm and 5 cm in the western and eastern part respectively (Fig. 1b). SSH anom-  
alies, averaged over three representative boxes in the northwestern (0° N–20° N, 130° E–150° E), southwestern (20° S–5° S,  
159° E–179° E) and eastern (7° S–3° N, 210° E–240° E) tropical Pacific (shown as red boxes 1–3 on the maps in Fig. 1), from  
observations and model simulation confirm the reduced amplitude of interannual variability by about 20%. However, the phase  
of the interannual variability is reproduced well, with correlation coefficients above 0.95 for all three boxes.

85

### 3 Results

Regional SSH variability is predominantly due to changes in the density of the water column (Fig. 2), with contributions from  
changes in the mass distribution negligible everywhere, except in shallow coastal regions (not shown). Fig. 2 shows the total

<sup>2</sup>We will refer to the sea level estimate of the OGCMs, which gives height above the geoid, as SSH

<sup>3</sup>[https://resources.marine.copernicus.eu/?option=com\\_csw&view=details&product\\_id=SEALEVEL\\_GLO\\_PHY\\_L4\\_REP\\_OBSERVATIONS\\_008\\_047](https://resources.marine.copernicus.eu/?option=com_csw&view=details&product_id=SEALEVEL_GLO_PHY_L4_REP_OBSERVATIONS_008_047)



SSH signal and its decomposition into steric, thermosteric and halosteric contributions for all three experiments. The steric signal in O025-HC is to a large extent due to changes in heat content (compare Fig. 2d and g). Compared to the total steric signal, the thermosteric variability shows slightly higher amplitudes in particular in the South Pacific Convergence Zone (SPCZ). The same area is characterized by elevated values of halosteric variability (Fig. 2j), reflecting a compensating effect of thermosteric and halosteric changes in the region.

The momentum flux experiments yield a very similar result. Here, total SSH variability is mostly due to heat content changes, with small contributions from halosteric changes that tend to dampen the thermosteric signal (compare Fig. 2b,e,h,k). Overall, these results concur with earlier accounts of the dominant role of thermosteric changes due to wind stress variability for SSH variability in the tropical Pacific.

However, although interannual SSH variability driven by surface buoyancy fluxes is small compared to the momentum flux driven variability, it is not negligible. Its spatial pattern differs from the wind stress driven component (Fig. 2c). The buoyancy flux contribution is most pronounced in the southern part of the study domain with its maximum in the central Pacific around  $10^{\circ}$  S and is lowest on the equator. The buoyancy flux driven signal is again steric in nature but in contrast to the wind stress driven signal the halosteric contribution is comparable in magnitude to the thermosteric part (compare Fig. 2 f, i and l).

In order to assess the interplay between momentum and buoyancy fluxes, we analyze the change in variability between the hindcast experiment O025-HC and the momentum flux experiment O025-W90. This allows us to identify regions where momentum and buoyancy fluxes are in phase and to assess whether they tend to amplify or dampen one another. Figure 3 shows the absolute change of interannual SSH variability in O025-W90 compared to O025-HC in terms of standard deviation (SD). Red/blue areas indicate regions where the variability increases/decreases when the interannual variability is removed from the buoyancy flux forcing, i.e. where buoyancy fluxes dampen/amplify wind stress driven SSH variability. The change in total SSH shows a pattern that is almost symmetrical about the equator (Fig. 3a). Negative values prevail around the equator and east of  $225^{\circ}$  E. A horseshoe shaped minimum is located at the eastern boundary. Positive values are centered at  $175^{\circ}$  E to both sides of the equator at  $10^{\circ}$  latitude. The same pattern can be seen for steric SSH (Fig. 3b) and, to a slightly lesser extent, for thermosteric SSH (Fig. 3c). The change in halosteric SSH is similar in magnitude but shows a different pattern. Changes are mainly limited to western and southwestern tropical Pacific where the halosteric SSH variability decreases in O025-W90. Buoyancy fluxes seem to have a small effect on halosteric SSH in the eastern to northeastern tropical Pacific. Notably, regions where halosteric SSH variability is increased coincide with regions where total steric variability is damped. This indicates again the compensating effect of halosteric SSH changes. In short, buoyancy fluxes tend to dampen SSH variability in the eastern part of the domain and amplify it in the central and western part of the region.

We take a closer look at two regions where buoyancy fluxes have a strong, but opposite effect and analyze spatial averages over the two boxes marked in Fig. 3. In the southwestern tropical Pacific, SSH changes driven by momentum and buoyancy



125 fluxes are clearly in phase but anticorrelated ( $p=-0.6$ ) on interannual to decadal timescales. This negative correlation corre-  
sponds to the damping effect of buoyancy fluxes identified before. The relative importance of buoyancy fluxes is strongest on  
decadal timescales, where it dampens the SSH variability by 20 % (Fig. 4a). Steric SSH variability in the eastern box shows  
similar amplitudes of interannual and decadal variability with the corresponding signals again being in phase, but this time  
positively correlated ( $p=0.7$ ). This is in line with the amplifying effect of buoyancy fluxes described above. In contrast to the  
western box, buoyancy fluxes have little effect on decadal SSH variability in the eastern part of the basin (Fig. 4b).

130

Figure 2 already indicates that both heat and freshwater fluxes drive SSH variability in particular in the region of the SPCZ.  
We investigate this further by decomposing SSH from O025-B90 into their thermosteric and halosteric parts again. Figure 5  
shows this decomposition for SSH anomalies in the southwestern and eastern tropical Pacific. In the southwestern domain (Fig.  
5a) steric SSH is influenced in equal parts by halosteric and thermosteric contributions from the beginning of the simulation  
135 until approximately 1990, after which the variability of thermosteric component decreases by more than 20% (SD drops from  
75 cm to 59 cm) and steric SSH is subsequently primarily controlled by halosteric SSH (SD of 0.76 cm throughout the in-  
tegration period). Steric SSH in the eastern equatorial Pacific is almost exclusively governed by thermosteric SSH. While its  
variability is also smaller during the later part of the simulation, the decrease is not as drastic as in the western box (SD reduces  
from 71 cm to 63 cm). Halosteric SSH shows only minor contributions, in particular during El Niño events (e.g. the 1997/98  
140 El Niño; SD of halosteric SSH increases from 20 cm to 25 cm between the two periods, which is due to this strong El Niño  
event).

The effect of buoyancy fluxes on SSH variability is uniform across the zonal extent of the tropical Pacific. This is in particu-  
lar true south of the equator and explains the opposite effect of buoyancy fluxes (i.e. damping in the west and amplification in  
145 the east) on the wind stress driven zonal dipole structure. Figure 6 shows the temporal evolution of SSH along a zonal section  
at  $10^\circ$  S. The dipole structure in thermosteric SSH is clearly visible in O025-HC and O025-W90 (Fig. 6a,b,d,e) whereas the  
effect of halosteric SSH in the same experiments is limited to the central and western part of the region (Fig. 6c,f). Its compen-  
sating effect, related to the adiabatic advection of warm and saline surface waters, is clearly visible. Negative SSH anomalies  
dominate in the western part of the area during the negative PDO phase in the 1980s and 90s and are caused by thermosteric  
150 anomalies. Positive halosteric anomalies act to increase SSH. SSH anomalies in O025-B90 show a zonally uniform structure  
across the basin (Fig.g-j), i.e their effect on the western and eastern poles of the wind stress driven, thermosteric dipole is  
exactly opposite. Maximum anomalies are located between  $200^\circ$  E and  $220^\circ$  E and are more pronounced in the western than in  
the eastern part of the area. The relative importance of buoyancy fluxes is highest for halosteric SSH, where amplitudes driven  
by momentum and buoyancy fluxes are comparable in magnitude (compare Fig 6f and i).

155

Our set of experiments specifically suggests that buoyancy–forced SSH variability in the tropical Pacific is relevant on in-  
terannual to decadal timescales. Since the early 1990s buoyancy flux driven SSH in the southwestern tropical Pacific is mostly  
controlled by halosteric effects with the strongest signals emerging during El Niño or La Niña events. In order to obtain insight



160 into the mechanism by which halosteric SSH anomalies are triggered by buoyancy fluxes, how they spread zonally and how they interact with the wind driven SSH anomalies during ENSO events, we examine the particularly strong El Niño event in 1997/98.

### 3.1 Case Study: 1997/98 El Niño

SSH anomalies from O025-HC during the El Niño event show the characteristic zonal dipole (Fig. 7a). In contrast to that, 165 O025-B90 shows positive SSH anomalies centered in the central basin at the beginning of 1998. These anomalies propagate westward with phase speeds of about  $17 \text{ cm s}^{-1}$ , which is in accordance with phase speeds of Rossby waves derived from linear theory (Killworth et al., 1997). These anomalies counteract the negative wind stress driven anomalies once they reach the western part of the domain by mid-1998 (Fig. 7b). These anomalies are mostly halosteric in nature (Fig. 7c). Areas of high precipitation start to propagate eastward at the beginning of 1997 and reach their easternmost position by the end of the 170 same year where they trigger the SSH anomalies (Fig. 7d). There are only small precipitation anomalies east of  $240^\circ \text{ E}$ , which explains the weak halosteric SSH anomalies in the eastern part of the basin described above. We note that the freshwater flux is controlled by precipitation at this latitude and evaporation is negligible (not shown). Thermosteric sea level anomalies are smaller than their halosteric counterpart (Fig. 7e) and heat flux anomalies do not show a coherent structure (Fig. 7f).

175 A different picture emerges along the equator. The zonal SSH dipole in O025-HC (Fig. 8a) is related to positive anomalies in the eastern basin, which are amplified by buoyancy fluxes (Fig. 8c). The steric anomalies are dominated by their thermosteric component (Fig. 8b,e), triggered by positive heatflux anomalies that evolve throughout the zonal extent of the basin after mid-1997 and early 1998 (Fig. 8f). Precipitation anomalies between mid-1997 and mid-1998 (Fig. 8d) are even stronger at the equator than at  $10^\circ \text{ S}$  but steric SSH anomalies in the central basin are weaker and we do not find a pronounced zonal propa- 180 gation of these anomalies. A possible reason is that sea level and thermocline depth expressions of Rossby waves are stronger off the equator, rendering signals of zonal propagation weaker on the equator. Another possible reason concerns the monthly resolution of the model output which is insufficient to show the adjustment process associated with the eastward propagation of Kelvin waves. Given phase speeds of  $2.8 \text{ m s}^{-1}$  for the first baroclinic mode (Gill, 1982), Kelvin waves would take about 45 days to cross the distance between the dateline and the American west coast.

185

In summary, positive SSH anomalies appear to be induced by buoyancy flux anomalies in the tropical Pacific during the peak of the El Niño event. Precipitation anomalies and collocated halosteric SSH anomalies suggest that fresh water fluxes play an important part in this mechanism. Off-equatorial SSH anomalies propagate westward as Rossby waves and counteract the negative SSH anomalies in the western tropical Pacific.



#### 190 4 Summary and conclusion

We used a global ocean model to run a set of sensitivity experiments to determine the impact of ocean–atmosphere buoyancy fluxes on interannual to decadal SSH variability in the tropical Pacific. As expected, wind stress variability, associated with the major basin–scale climate modes, is the most important driver of SSH variability in the region, causing the well known zonal dipole with opposing tendencies of SLC in the western and eastern parts of the tropical Pacific. We find that SSH variability  
195 due to buoyancy fluxes is generally small but not negligible, with strongest contributions around 10° N/S and a maximum in standard deviation of 2 cm in the central portion of the south Pacific.

Previous studies based on sensitivity experiments (Piecuch and Ponte, 2012; Forget and Ponte, 2015; Meyssignac et al., 2017) tend to agree with the results presented here in that they find a maximum of buoyancy flux forced interannual SSH  
200 variability on the order of 2–3 cm in the central tropical Pacific south of the equator. Studies using different methods, including budget analyses of ocean state estimates, identified an impact of buoyancy flux forcing mostly in the western tropical Pacific (Piecuch and Ponte, 2011; Fukumori and Wang, 2013), with amplitudes of the related sea level variability of up to 10 cm. However, all previous studies were limited to a period of 2–3 decades, i.e., the altimetric period since 1992.

205 By building on model simulations over the last six decades, the present study provides an extended perspective on the variability on interannual time scales and also allows a view on the decadal-scale changes. While previous studies mostly focus on heat fluxes we also analysed the importance of fresh water fluxes for steric sea level anomalies.

The results of the sensitivity experiments presented here suggest that, in contrast to the prevailing wind stress driven zonal  
210 dipole, buoyancy flux driven sea level variability is zonally uniform across the extent of the basin but varies in phase with the wind stress driven part. More specifically, buoyancy fluxes tend to dampen SSH variability in the western part of the basin but amplify it in the east. The eastern part of the domain is mostly dominated by interannual heat flux variability that increases during El Niño events, thereby increasing the thermosteric SSH and amplifying positive sea level anomalies in the region. Here, buoyancy forcing has no impact on the variability on decadal timescales. Halosteric sea level variability driven by buoyancy  
215 fluxes is negligible in this area since its variability is largely confined to the central and western parts of the domain. In contrast, steric SSH variability due to surface buoyancy fluxes in the central and western Pacific is equally affected by thermosteric and halosteric contributions, with an increasing, relative importance of halosteric SSH in the last three decades due to a reduction of thermosteric SSH variability by more than 20%. Overall, buoyancy fluxes contribute to SSH variability on both interannual and decadal timescales, with a higher relative importance for the latter where they dampen the wind stress driven signal by 20%.

220

The example of the 1997/98 El Niño event illustrates the oceanic response to buoyancy forcing. Halosteric SSH anomalies are induced in the central tropical Pacific by strong precipitation anomalies during El Niño events and propagate westward as off–equatorial Rossby waves, where they act to dampen negative, thermosteric SSH anomalies. The oceanic response to



225 buoyancy forcing can therefore be regarded as a dynamical signal, that allows local buoyancy flux anomalies to remotely impact SSH. The mechanism appears similar to that described by Piecuch and Ponte (2012), suggesting a robust result of model sensitivity experiments to probe the relative importance of different forcing components. The contribution of both heat and freshwater fluxes identified here also emphasises the need for an accurate representation of all components of the local air-sea buoyancy fluxes in model studies of regional sea level projections in the tropical Pacific.

*Data availability.* Data shown in this paper are available at <http://data.geomar.de>

230 *Author contributions.* PW and CB defined the overall research problem and methodology; PW and MS developed, ran, and validated the OGCM experiments ; PW produced all figures; PW prepared the paper with contributions from all coauthors.

*Competing interests.* The authors declare that they have no conflict of interest.

235 *Acknowledgements.* PW was supported by the Deutsche Forschungsgemeinschaft (DFG) as part of the Special Priority Program (SPP)–1889 "Regional Sea Level Change and Society" (Grant BO907/5-1). All model simulations have been performed at the North–German Supercomputing Alliance (HLRN).



## References

- Barnier, B., Madec, G., Penduff, T., Molines, J. M., Treguier, A. M., Le Sommer, J., Beckmann, A., Biastoch, A., Böning, C., Dengg, J., Derval, C., Durand, E., Gulev, S., Remy, E., Talandier, C., Theetten, S., Maltrud, M., McClean, J., and De Cuevas, B.: Impact of partial steps and momentum advection schemes in a global ocean circulation model at eddy-permitting resolution, *Ocean Dynamics*, 56, 543–567, <https://doi.org/10.1007/s10236-006-0082-1>, 2006.
- Fichefet, T. and Maqueda, M. A. M.: Sensitivity of a global sea ice model to the treatment of ice thermodynamics and dynamics, *Journal of Geophysical Research: Oceans*, 102, 12 609–12 646, <https://doi.org/10.1029/97JC00480>, 1997.
- Forget, G. and Ponte, R. M.: The partition of regional sea level variability, *Progress in Oceanography*, 137, 173–195, <https://doi.org/10.1016/j.pocean.2015.06.002>, 2015.
- Fukumori, I. and Wang, O.: Origins of heat and freshwater anomalies underlying regional decadal sea level trends, *Geophysical Research Letters*, 40, 563–567, <https://doi.org/10.1002/grl.50164>, 2013.
- Gill, A. E.: *Atmosphere-ocean dynamics*, Academic Press, New York, 1982.
- Killworth, P. D., Chelton, D. B., and De Szoeke, R. A.: The speed of observed and theoretical long extratropical planetary waves, *Journal of Physical Oceanography*, 27, 1946–1966, [https://doi.org/10.1175/1520-0485\(1997\)027<1946:TSOAT>2.0.CO;2](https://doi.org/10.1175/1520-0485(1997)027<1946:TSOAT>2.0.CO;2), 1997.
- Madec, G. and NEMO-team: NEMO ocean engine, Tech. rep., Institut Pierre-Simon Laplace (IPSL), Paris, 2016.
- McGregor, S., Timmermann, A., Schneider, N., Stuecker, M. F., and England, M. H.: The effect of the south pacific convergence zone on the termination of el niño events and the meridional asymmetry of ENSO, *Journal of Climate*, 25, 5566–5586, <https://doi.org/10.1175/JCLI-D-11-00332.1>, 2012.
- Merrifield, M. A.: A shift in western tropical Pacific sea level trends during the 1990s, *Journal of Climate*, 24, 4126–4138, <https://doi.org/10.1175/2011JCLI3932.1>, 2011.
- Merrifield, M. A. and Maltrud, M. E.: Regional sea level trends due to a Pacific trade wind intensification, *Geophysical Research Letters*, 38, 1–5, <https://doi.org/10.1029/2011GL049576>, 2011.
- Merrifield, M. A., Thompson, P. R., and Lander, M.: Multidecadal sea level anomalies and trends in the western tropical Pacific, *Geophysical Research Letters*, 39, 2–6, <https://doi.org/10.1029/2012GL052032>, 2012.
- Meysignac, B., Piecuch, C. G., Merchant, C. J., Racault, M., Palanisamy, H., Macintosh, C., Sathyendranath, S., and Brewin, R.: Causes of the Regional Variability in Observed Sea Level , Sea Surface Temperature and Ocean Colour Over the Period 1993 – 2011, *Surveys in Geophysics*, 38, 187–215, <https://doi.org/10.1007/s10712-016-9383-1>, 2017.
- Moon, J. H. and Tony Song, Y.: Sea level and heat content changes in the western North Pacific, *Journal of Geophysical Research: Oceans*, 118, 2014–2022, <https://doi.org/10.1002/jgrc.20096>, 2013.
- Moon, J. H., Song, Y. T., Bromirski, P. D., and Miller, A. J.: Multidecadal regional sea level shifts in the Pacific over 1958–2008, *Journal of Geophysical Research: Oceans*, 118, 7024–7035, <https://doi.org/10.1002/2013JC009297>, 2013.
- Piecuch, C. G. and Ponte, R. M.: Mechanisms of interannual steric sea level variability, *Geophysical Research Letters*, 38, 1–6, <https://doi.org/10.1029/2011GL048440>, 2011.
- Piecuch, C. G. and Ponte, R. M.: Buoyancy-driven interannual sea level changes in the southeast tropical Pacific, *Geophysical Research Letters*, 39, 1–5, <https://doi.org/10.1029/2012GL051130>, 2012.
- Piecuch, C. G., Thompson, P. R., and Hamlington, B. D.: What Caused Recent Shifts in Tropical Pacific Decadal Sea-Level Trends ?, *Journal of Geophysical Research: Oceans*, 124, <https://doi.org/10.1029/2019JC015339>, 2019.



- Qiu, B. and Chen, S.: Multidecadal Sea Level and Gyre Circulation Variability in the Northwestern Tropical Pacific Ocean, *Journal of Physical Oceanography*, 42, 193–206, <https://doi.org/10.1175/JPO-D-11-061.1>, 2012.
- 275 Ryan, S., Ummerhofer, C. C., Gawarkiewicz, G., Wagner, P., Scheinert, M., Biastoch, A., and Böning, C. W.: Depth structure of Ningaloo Niño/Niña events and associated drivers, *Journal of Climate*, pp. 1767–1788, <https://doi.org/10.1175/jcli-d-19-1020.1>, 2021.
- Stammer, D., Cazenave, A., Ponte, R. M., and Tamisiea, M. E.: Causes for Contemporary Regional Sea Level Changes, *Annual Review of Marine Science*, 5, 21–46, <https://doi.org/10.1146/annurev-marine-121211-172406>, 2013.
- Stewart, K. D., Kim, W. M., Urakawa, S., Hogg, A. M. C., Yeager, S., Tsujino, H., Nakano, H., Kiss, A. E., and Danabasoglu, G.: JRA55-do-based repeat year forcing datasets for driving ocean–sea-ice models, *Ocean Modelling*, 147, 101557, <https://doi.org/10.1016/j.ocemod.2019.101557>, 2020.
- 280 Timmermann, A., McGregor, S., and Jin, F. F.: Wind effects on past and future regional sea level trends in the southern Indo-Pacific, *Journal of Climate*, 23, 4429–4437, <https://doi.org/10.1175/2010JCLI3519.1>, 2010.
- Tsujino, H., Urakawa, S., Nakano, H., Small, R. J., Kim, W. M., Yeager, S. G., Danabasoglu, G., Suzuki, T., Bamber, J. L., Bentsen, M., Böning, C. W., Bozec, A., Chassignet, E. P., Curchitser, E., Boeira Dias, F., Durack, P. J., Griffies, S. M., Harada, Y., Ilicak, M., Josey, S. A., Kobayashi, C., Kobayashi, S., Komuro, Y., Large, W. G., Le Sommer, J., Marsland, S. J., Masina, S., Scheinert, M., Tomita, H., Valdivieso, M., and Yamazaki, D.: JRA-55 based surface dataset for driving ocean–sea-ice models (JRA55-do), *Ocean Modelling*, 130, 79–139, <https://doi.org/10.1016/j.ocemod.2018.07.002>, 2018.
- 285 Ummerhofer, C. C., Ryan, S., England, M. H., Scheinert, M., Wagner, P., Biastoch, A., and Böning, C. W.: Late 20th Century Indian Ocean Heat Content Gain Masked by Wind Forcing, *Geophysical Research Letters*, 47, 1–10, <https://doi.org/10.1029/2020GL088692>, 2020.
- 290 Zanna, L., Khatiwala, S., Gregory, J. M., Ison, J., and Heimbach, P.: Global reconstruction of historical ocean heat storage and transport, *Proceedings of the National Academy of Sciences*, 116, 1126–1131, <https://doi.org/10.1073/pnas.1808838115>, 2019.

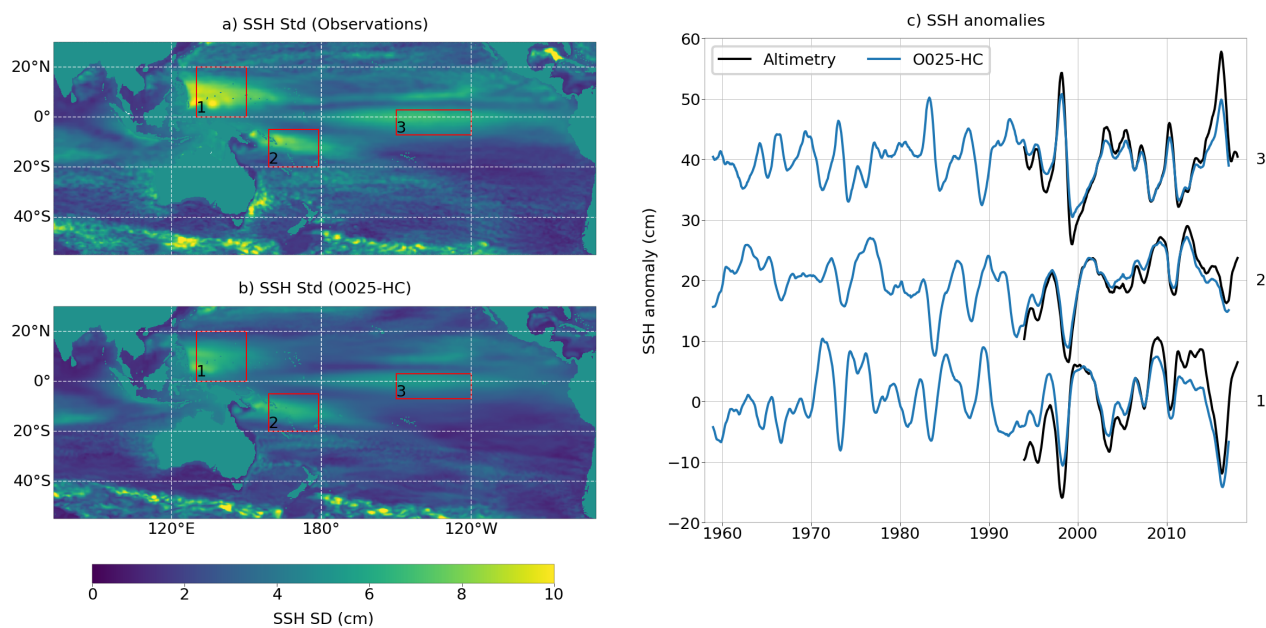


**Figure 1.** Interannual SD of SSH from (a) observations and (b) model simulation O025-HC. (c) SSH anomalies from observations and O025-HC averaged over three areas indicated by red boxes on the maps. Note that in panel a constant offset of 20 cm and 40 cm was added to anomalies from box 2 and 3 respectively. The global mean trends have been subtracted and all timeseries are smoothed with a 12-month running mean.

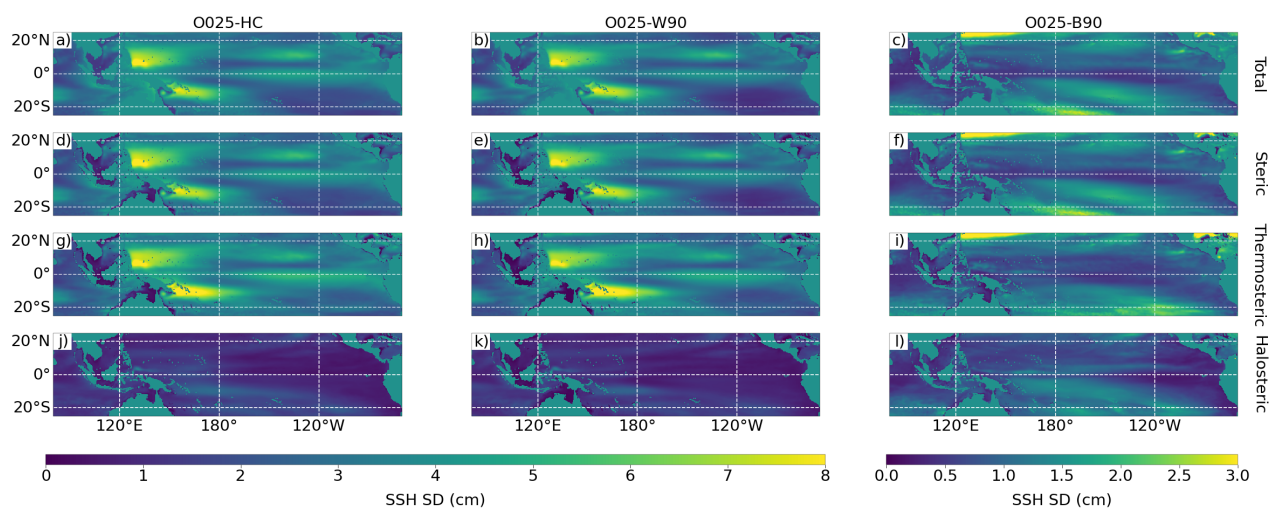


**Figure 2.** Interannual SD of total SSH (first row), steric SSH (second row), thermosteric SSH (third row) and halosteric SSH (fourth row) from O025-HC (left), Wind90 (middle) and Buoy90 (right).

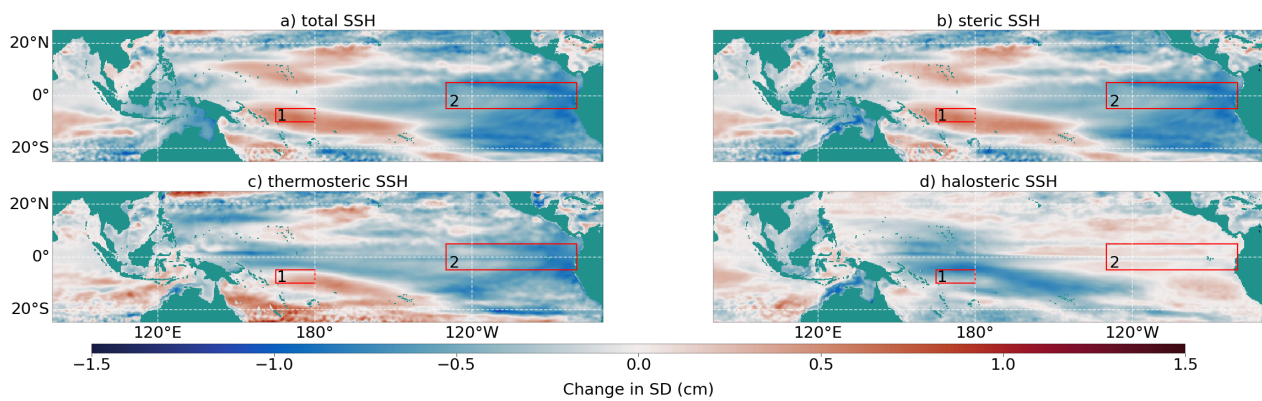


**Figure 3.** Difference in interannual SD between O025-HC and O025-W90 for (a) total SSH, (b) steric SSH, (c) thermosteric SSH and (d) halosteric SSH.

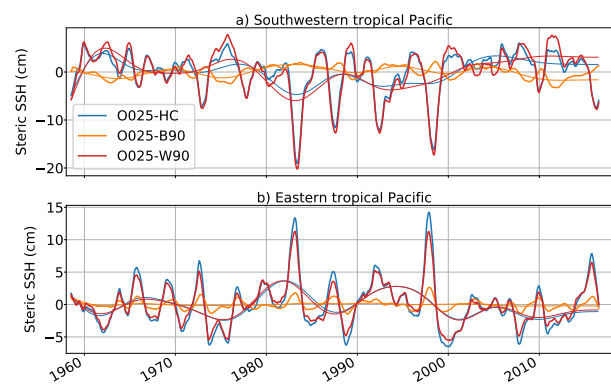


**Figure 4.** Timeseries of steric SSH anomalies from O025-HC, O025-W90 and O025-B90 averaged over boxes in the (a) southwestern and (b) eastern tropical Pacific. Exact regions are shown as red boxes (1,2) in Fig. 3. Thick lines are smoothed with a 12-year running mean. Thin lines are low-pass filtered with a 8-year butterworth filter.

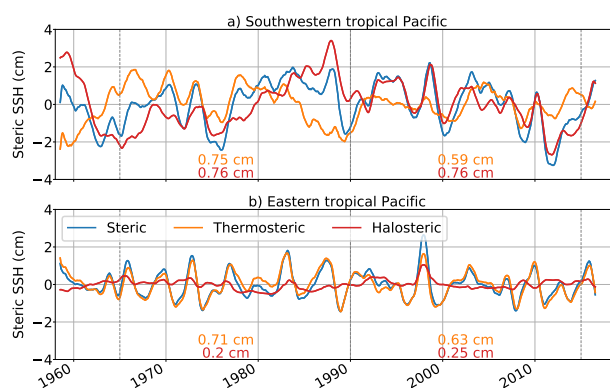


**Figure 5.** Timeseries of steric SSH anomalies from O025-B90 averaged over boxes in the (a) southwestern and (b) eastern tropical Pacific. Exact areas are shown as boxes 1 and 2 respectively in Fig. 3. Standard deviations for thermosteric and halosteric SSH anomalies are given for the periods from 1965–1990 and 1990–2015. All time series are smoothed with a 12-year running mean.

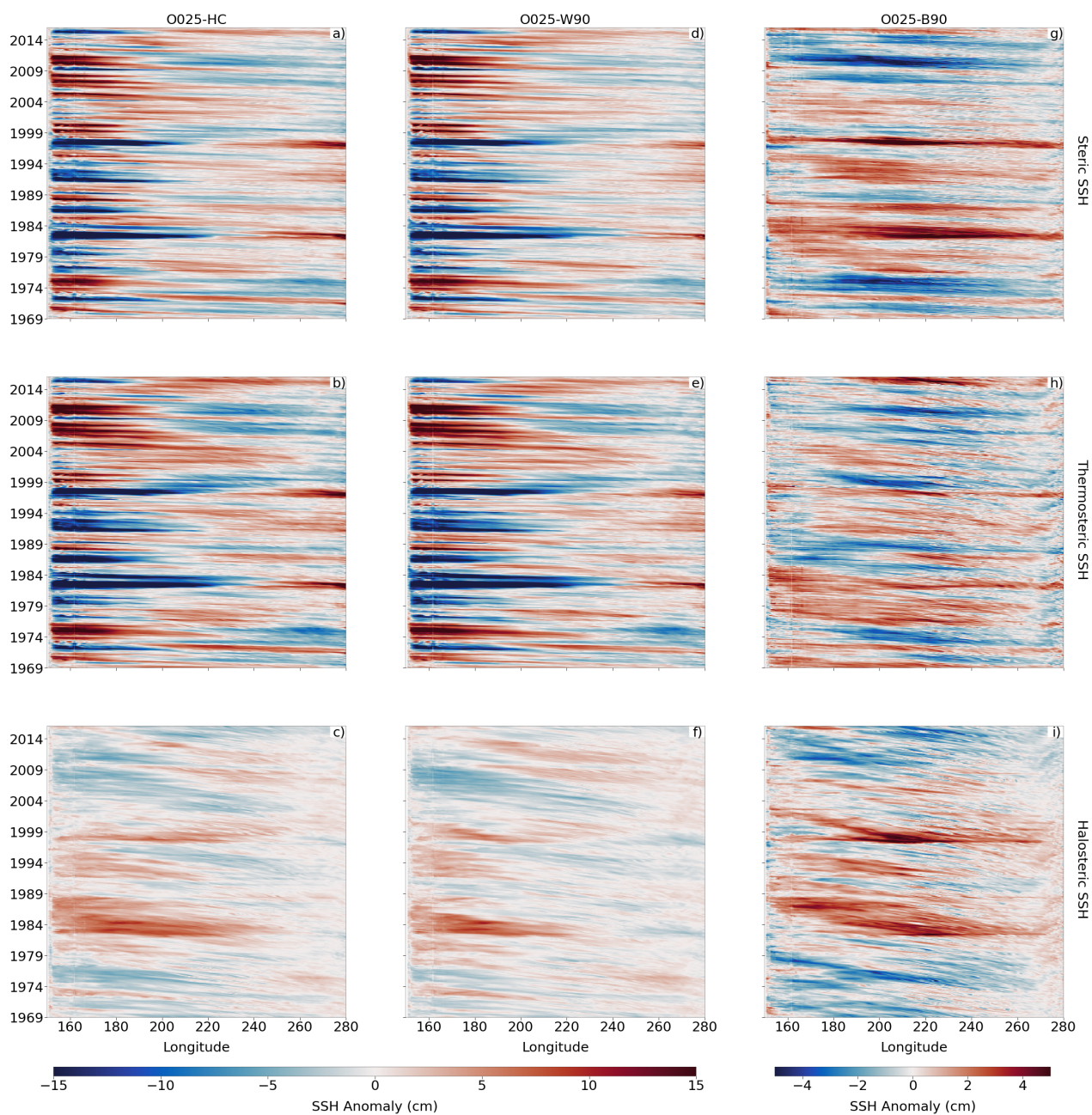


**Figure 6.** Hovmöller diagram of SSH anomalies at  $10^{\circ}$  S. Steric SSH (first row), thermosteric SSH (second row) and halosteric SSH (third row) from O025-HC (left), O025-W90 (middle) and O025-B90 (right). All data has been smoothed with a 12-month running mean.

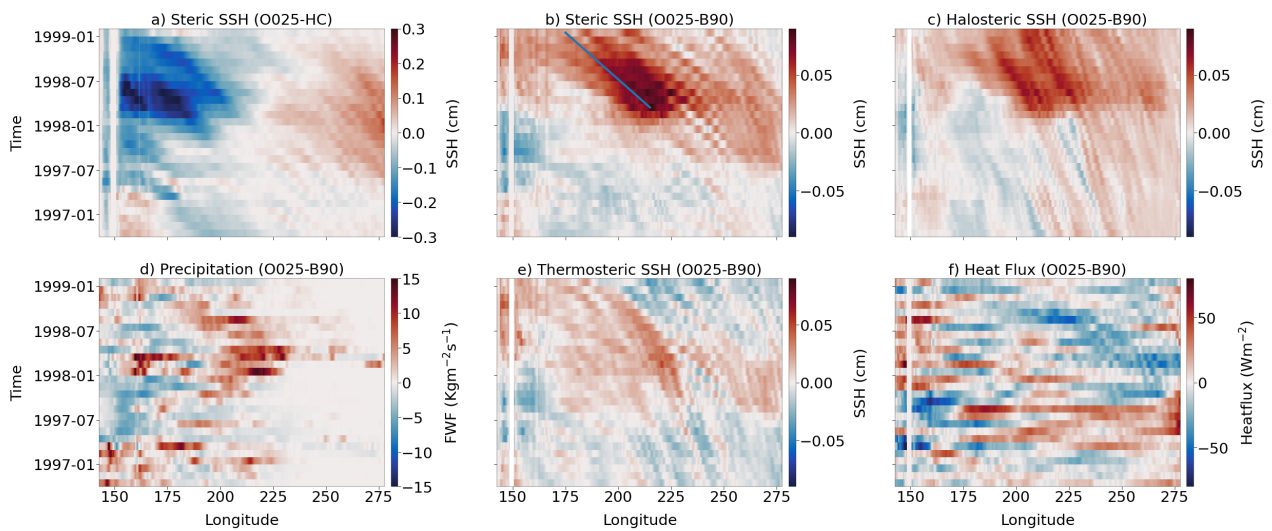


**Figure 7.** Hovmöller diagram at 10° S. (a) Anomalies of steric SSH from O025-HC and anomalies from O025-B90 of (b) steric SSH, (c) halosteric SSH, (d) precipitation, (e) thermosteric SSH and (f) net downward heatflux.

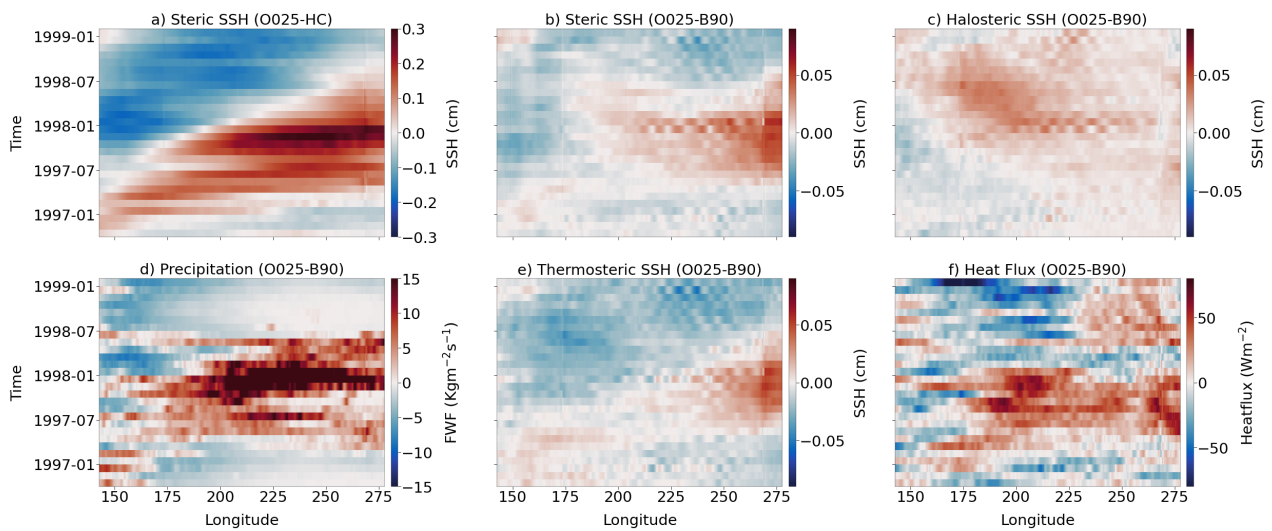


**Figure 8.** Hovmöller diagram at the equator. (a) Anomalies of steric SSH from O025-HC and anomalies from O025-B90 of (b) steric SSH, (c) halosteric SSH, (d) precipitation, (e) thermosteric SSH and (f) net downward heatflux.